The Astrophysical Journal Letters, 971:L1 (9pp), 2024 August 10 https://doi.org/10.3847/2041-8213/ad62f8

Observations of Locally Excited Waves in the Low Solar Atmosphere Using the Daniel K. Inouye Solar Telescope

Shah Mohammad Bahauddin[1,2], Catherine E. Fischer[3], Mark P. Rast[1,4], Ivan Milic[5], Friedrich Woeger[3], Matthias Rempel[6], Peter H. Keys[7], and Thomas R. Rimmele[3]
[1] Laboratory for Atmospheric and Space Physics, University of Colorado, Boulder, CO 80303, USA; shahmohammad.bahauddin@colorado.edu
[2] DKIST Ambassador, National Solar Observatory, Boulder, CO 80303, USA
[3] National Solar Observatory, Boulder, CO 80309, USA
[4] Department of Astrophysical and Planetary Sciences, University of Colorado, Boulder, CO 80309, USA
[5] Leibniz-Institut für Sonnenphysik, Freiburg im Breisgau, Germany
[6] High Altitude Observatory, NSF National Center for Atmospheric Research, Boulder, CO 80307, USA
[7] Astrophysics Research Centre, School of Mathematics and Physics, Queen's University Belfast, Belfast, BT7 1NN, UK

Received 2024 March 20; revised 2024 June 26; accepted 2024 June 26; published 2024 August 6

Abstract

We present an interpretation of the recent Daniel K. Inouye Solar Telescope (DKIST) observations of propagating wave fronts in the lower solar atmosphere. Using MPS/University of Chicago MHD radiative magnetohydrodynamic simulations spanning the solar photosphere, the overshoot region, and the lower chromosphere, we identify three acoustic-wave source mechanisms, each occur at a different atmospheric height. We synthesize the DKIST Visible Broadband Imager *G*-band, blue-continuum, and Ca II *K* signatures of these waves at high spatial and temporal resolution, and conclude that the wave fronts observed by DKIST likely originate from acoustic sources at the top of the solar photosphere overshoot region and in the chromosphere proper. The overall importance of these local sources to the atmospheric energy and momentum budget of the solar atmosphere is unknown, but one of the excitation mechanisms identified (upward propagating shock interaction with down-welling chromospheric plasma resulting in acoustic radiation) may be an important shock dissipation mechanism. Additionally, the observed wave fronts may prove useful for ultralocal helioseismological inversions and promise to play an important diagnostic role at multiple atmospheric heights.

Unified Astronomy Thesaurus concepts: The Sun (1693); Quiet sun (1322); Solar oscillations (1515)

Materials only available in the online version of record: animations

1. Introduction

Investigating the low solar atmosphere, from the deep photosphere to the low chromosphere, is central to understanding the transfer of mass and energy from the solar interior to the corona. Given the prevalence of acoustic waves in this region, understanding their source, propagation, and dissipation is crucial. Moreover, high-resolution observations of these waves have significant diagnostic potential.

The study of solar acoustic waves has a history of several decades, with theoretical analyses suggesting that these waves originate from discrete dynamical events both within and below the solar photosphere. They are responsible for the resonant global *p*-modes, and their high-frequency components propagate upward into the solar atmosphere, potentially contributing to momentum deposition and heating (e.g., Biermann 1946; Schwarzschild 1948; Hansteen et al. 2006; Kalkofen 2007; Abbasvand et al. 2020; Yadav et al. 2021; Molnar et al. 2023 and references therein). Various mechanisms for exciting solar acoustic waves have been proposed (e.g., Lighthill 1952, 1954; Stein 1967, 1991; Goldreich et al. 1994; Musielak et al. 1994; Rast 1995, 1999; Samadi & Goupil 2001; Samadi et al. 2007; Kitiashvili et al. 2019; Zhou et al. 2019, 2020; Philidet et al. 2021, 2022), with sporadic observational support for different mechanisms (e.g., Rimmele et al. 1995; Chaplin et al. 1998; Goode et al. 1998; Straus et al. 1999; Skartlien & Rast 2000; Strous et al. 2000; Severino et al. 2001; Bello González et al. 2010; Roth et al. 2010; Lindsey & Donea 2013; Lindsey et al. 2020). However, it remains unclear which mechanism is dominant, how well each couples to global *p*-modes, and which is most important for generating the high-frequency waves that contribute to atmospheric heating.

Accurate identification and characterization of solar acoustic sources necessitates careful separation of the source and the local wavefield from the background convective flows and *p*-modes. This is difficult because the amplitudes of the individual sources and the waves they emit are typically much smaller than those of the granulation and the *p*-mode coherence patches. The signal-to-noise ratio (SNR) of the locally generated wavefield to the background is typically well below unity, and the spectral content of the source signal overlaps with that of the *p*-modes and, to some extent, the background granular motions. Furthermore, the spatial extent of the waves and their propagation speed dictate the need for imaging instruments with exceptionally high spatial resolution (<40 km) and high temporal cadence ($\Delta t < 5$ s). Consequently, direct observation of the local acoustic-source wavefield remains challenging and has only recently been achieved in simulations by leveraging the timescale difference between the source-induced propagating wave fronts and background contributions (Bahauddin & Rast 2021, 2023) and in observations (Fischer et al. 2023) by employing the high-cadence high-resolution capabilities of the NSF's Daniel K. Inouye Solar Telescope (DKIST; Rimmele et al. 2020).

During the DKIST Operations Commissioning Phase Cycle 1, substantial effort was invested in taking high-resolution images of the low solar atmosphere with the Visible Broadband Imager (VBI; Wöger et al. 2021) in several wavelength channels. The nominal formation heights of the filtergrams acquired span from the base of the photosphere to the midchromosphere. Some of the time series show evidence of propagating wave fronts (Fischer et al. 2023), potentially originating from local acoustic sources. The wave fronts are not seen in a midphotospheric channel (*G*-band) but are visible in a channel with contributions from the upper photosphere and lower chromosphere (Ca II *K* band). As referenced above, most models of chromospheric waves have focused on waves generated below the photosphere, the high-frequency tail of the solar *p*-modes, or because of their signature in the *p*-mode spectra (e.g., Gabriel 1995; Nigam et al. 1998; Rast & Bogdan 1998; Skartlien & Rast 2000), on sources in the low photosphere (with the Solar Dynamics Observatory Helioseismic and Magnetic Imager's Fe I 617.3 nm and the Solar and Heliospheric Observatory Michelson Doppler Imager's Ni I 676.8 nm lines nominally forming at heights of 100 and 125 km above $\tau_{500} = 1$ respectively; Fleck et al. 2011). In contrast, these new observations and the analysis presented in this Letter reveal that numerous acoustic excitation events may occur much higher in the atmosphere, at the top of the photospheric overshoot region and in the low chromosphere.

We report here on propagating wave fronts observed in the DKIST/VBI Ca II *K* image time series that appear to emanate from local acoustic events. We support the interpretation of their origin as local by comparing the observed properties of the wave fronts with those of similar events found in MPS/University of Chicago Radiative MHD (MURaM; Vögler et al. 2005; Rempel et al. 2009; Rempel 2014) simulations of the lower solar atmosphere. Analogous wave sources in the simulated atmosphere are located in the upper photosphere and lower chromosphere, and forward modeled spectra of the DKIST/VBI observational channels confirm the visibility of the wave fronts generated by these sources in Ca II *K* filtergrams but not in the *G* band. The combined evidence from observations and numerical simulations suggests that acoustic-wave sources are ubiquitous in the low solar atmosphere.

2. DKIST Observations

We present an analysis of the quiet-Sun image time series from the DKIST/VBI spanning 17:46 UTC to 19:31 UTC of 2022 May 26 (Dataset ID: AQKXV, AOLZW). The centers of the two regions observed (in helioprojective coordinates) lie at the disk center, both with a field of view of $45''.06 \times 45''.06$. The primary observations we employ are the time series taken in the Ca II *K* (center wavelength (CWL): 393.327 nm; full width at half-maximum (FWHM): 0.101 nm) and *G*-band (CWL: 430.52 nm; FWHM: 0.437 nm) channels.

Because of atmospheric turbulence and the variable seeing conditions during the observations, the quality of the images differs across the fields of view (FOVs), and the clearest portion of the FOV at any given time does not necessarily coincide with the location of wave front propagation. In our study, of the nearly 2 hr of observation, we could identify approximately 15 minutes where a small portion of the VBI's FOV overlapped with the wave front propagation area, yielding wave front data with the highest quality and resolution.

For the whole time series, the VBI camera collected bursts of images at 30 Hz, alternating between the Ca II *K* and *G*-band channels. Short exposures, adaptive optics, and speckle reconstruction (based on the KISIP code of Wöger et al. 2008) were combined to yield image time series with 6 s cadence, in both the Ca II *K* and the *G* band, and spatial sampling (pixel scale) of $0''.011$. The images show an approximately 40-pixel spatial shift between the two channels; this shift was accounted for when the $17''.6 \times 15''.4$ area was extracted for image postprocessing and analysis. We note that these broadband images (0.1 and 0.437 nm passband for Ca II *K* and the *G* band respectively) are not sensitive to the line-of-sight (LOS) velocities since typical $v_{\rm LOS}$ in the low solar atmosphere is less than $10\ {\rm km\ s^{-1}}$ (or 0.015 nm Doppler shifts). Therefore, the wave front motions described below are discernible due to thermodynamic perturbations induced by the wave within the atmospheric regions that contribute to each passband.

The strong Ca II *K* resonant line we observe is frequently used for broadband characterization of solar and stellar activity. The line covers a wide range of wavelengths, with formation heights ranging from the photosphere to the midchromosphere (from $\tau_{500} = 1$ to about 1500 km height). The Ca II *K* channel of the DKIST/VBI is centered at the line (393.327 nm) with a width of 0.1 nm, and thus primarily samples the chromosphere, though it also includes contributions from the upper photosphere (down to a height of about 400 km; e.g., Ermolli et al. 2010).

Opacity in the *G* band arises from the absorption due to the presence molecules, primarily the CH (methylidyne) molecule. It exhibits larger contrast than pure continuum because the molecule number densities depend strongly on the temperature. With a passband of 0.437 nm, the VBI *G*-band channel probes photospheric regions from slightly above the blue continuum (a height of approximately 100 km) to the temperature minima (e.g., Hansteen et al. 2009). *G*-band images typically capture fine details of the photosphere, including granular substructure and magnetic bright points.

2.1. Locally Excited Wave Fronts in DKIST/VBI Data

Inspection of the image time series captured by the DKIST VBI in the Ca II *K* channel reveals spatially compact and temporally discrete propagating wave fronts similar to those reported in Fischer et al. (2023). However, the waves examined in this study do not originate from magnetic bright points, nor do they produce the shock fronts, primarily described in Fischer et al. (2023). Instead, these waves exhibit a more hydrodynamic nature, suggesting that while their source mechanisms might be influenced by the magnetic environment, their propagation is primarily dictated by pressure perturbations. These transient events can be identified against the high amplitude, relatively slowly varying background flows because they are spatially resolved and because the temporal cadence of the observations is high enough to capture their propagation. The amplitudes of the transients are just marginally higher than the variance of the background granular flows and *p*-mode coherence patches (SNR is slightly over one). Consequently, the wave fronts are readily discernible when viewing image time series but their identification and characterization in any single image is difficult. Because of the inherent timescale differences between the signal (the wave front perturbation) and the background, temporal-difference filtering can significantly improve wave front SNR in simulations (Bahauddin & Rast 2021, 2023), but this method does not work well on this ground-based observational time

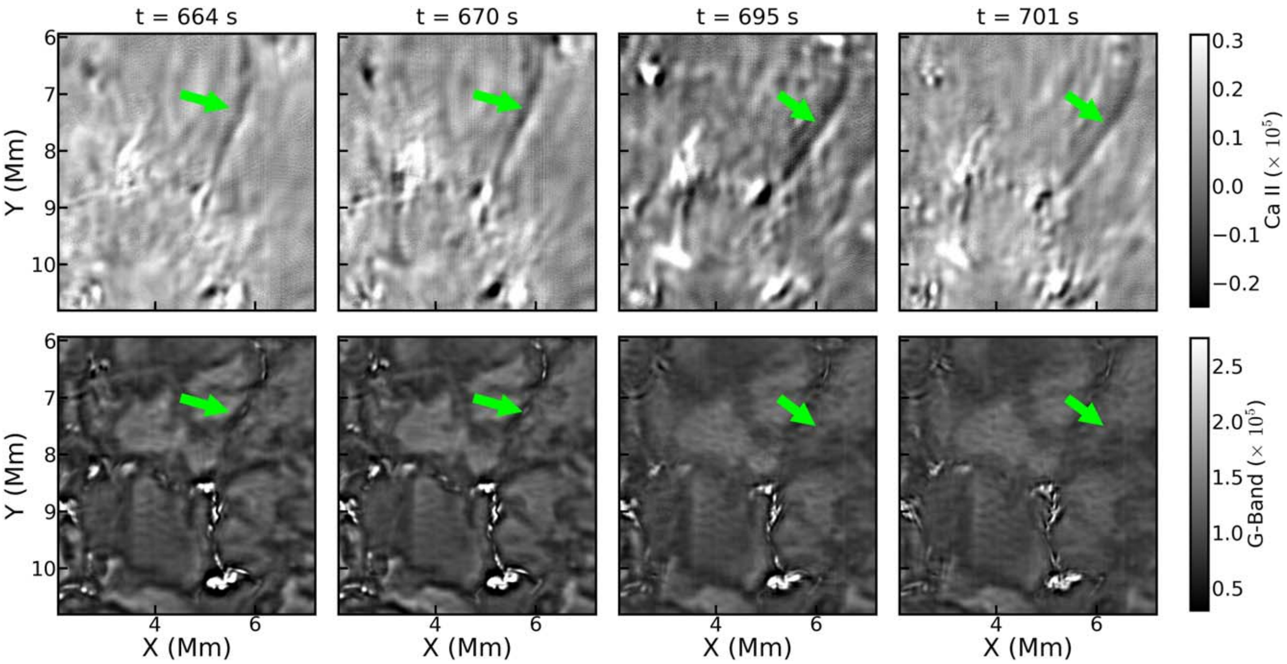

Figure 1. DKIST/VBI observations of wave front propagation in the Ca II *K* and corresponding G-band channels. The top row displays the time sequence of Ca II *K* images with unsharp masking applied for contrast enhancement. The green arrow highlights the position of the wave front. The bottom row presents the same time sequence in the *G*-band channel. No discernible wave front is visible in *G*-band images even with unsharp masking, with the green arrows indicating where the wave fronts would be in the time series shown. This time series is delayed by 140 s relative to that of Ca II *K* in order to account for the travel time of the waves between the photosphere and the low chromosphere. Other delays were also examined, which are described in the text and can be seen in the animation. The time series shown in the animation is 894 s and the real-time duration of the video is 30 s.

(An animation of this figure is available in the online article.)

series due to variations in image brightness between consecutive frames. Instead, we employ unsharp masking (IDL code `UNSHARP_MASK`; for Ca II *K*, `AMOUNT = 20, RADIUS = 5` and for the *G* band, `AMOUNT = 3, RADIUS = 5`) to enhance the contrast along the edges of wave front perturbations. Such a contrast enhanced image time series is shown in Figure 1, with Ca II *K* images along the top row and *G*-band images along the bottom. A video of the time series is hosted by Figure 1 in the online journal.

The green arrow in the upper row of images in Figure 1 indicates the position of an observed wave front propagating away from a source site in the Ca II *K* time series. The wave front has a width of about 0.″4 (∼300 km), extends about 3 Mm, and propagates with a speed of about 14 km s^{-1}. Surprisingly, no discernible wave front is visible in coaligned *G*-band images (bottom row in Figure 1), either cotemporally or staggered earlier or later in time. The *G*-band images were examined for the presences of propagating wave fronts for times spanning several minutes before and after their initial appearance in the Ca II *K* images. This time frame (approximately ∼140 s) is the approximate travel time of acoustic waves between the formation heights of the passbands, estimated by integrating the sound speed from the photospheric surface to a height of 1000 km above it in a realistically simulated photosphere (simulations details in Section 3). The investigation covers both forward and backward temporal directions due to the uncertainty regarding whether the wave initiates in the photosphere and then propagates to the chromosphere or vice versa. The absence of the wave front in the *G*-band images is true of all Ca II *K* events observed (an additional event is illustrated in the animation hosted by Figure 1), and suggests that the wave front perturbations seen in the DKIST VBI Ca II *K* data originate in the chromosphere and do not travel downward into or upward from the photosphere. This is supported by analysis of similar wave fronts found in magnetohydrodynamic (MHD) simulations.

3. Locally Excited Wave Fronts in a Simulated Atmosphere

We study a MURaM simulation of solar convection with physical dimension $L_x \times L_y \times L_z = 6.144 \times 6.144 \times 4.096$ Mm^3, where L_z specifies the vertical direction. The domain has uniform 16 km grid spacing in all directions. It extends for 1 hr of solar time, with output saved every 2.0625 s. The data cube thus has the native dimensions $1800 \times 384 \times 384 \times 256$. The top boundary of the simulation is located 1.7 Mm above mean $\tau_{500} = 1$ and the depth of the convective portion of the layer below that is 2.3 Mm. Horizontally periodic boundary conditions were employed in the solution, along with a semitransparent upper boundary (closed for downflows and opened for upflows) and an open lower boundary (mass preserving). For reference, the simulation is a rerun of Simulation O16b from Rempel (2014), with nongray radiative transfer (four opacity bins; e.g., Nordlund 1982; Perdomo García et al. 2023) and a domain extended an additional 1.024 Mm upwards. The simulation computes the radiation field under the assumption of local thermodynamic equilibrium (LTE).

3.1. DKIST/VBI Synthesis

MHD quantities such as temperature, velocity, and gas pressure, cannot be readily determined from the DKIST/VBI image time series. To relate the MURaM models to the observations, we forward modeled the observed passbands, Ca II *K* and *G*-band. Although no simultaneous continuum observations were taken, we also synthesized the DKIST/VBI blue-continuum channel, as this band probes physical conditions near the base of the photosphere ($\tau_{500} = 1$ in semiempirical models such as FALC; Fontenla et al. 1993) and the presence or absence of wave front signal there in the simulations may be useful in designing follow up studies.

The *G*-band spectra is modeled using the Rybicki–Hummer (RH) radiative transfer code (Uitenbroek 2001), and the blue-continuum and Ca II *K* spectra using the Spectropolarimetric NLTE inversion (SNAPI) radiative transfer code (Milić & van Noort 2018). Both codes employ the multilevel accelerated lambda iteration formalism (Rybicki & Hummer 1991) to solve for atomic level populations in non–local thermodynamic equilibrium (NLTE). The *G*-band wavelengths were synthesized under the LTE assumption, whereas the Ca II *K* wavelengths were synthesized considering NLTE ionization of hydrogen and complete frequency redistribution in the line. Both bandpasses were synthesized for a set of densely sampled wavelengths ±2 nm around the bandpass center, multiplied by the VBI filter profiles, and integrated over wavelength, to emulate the observations.

In the subsequent sections, we present evidence from the MURaM simulated atmosphere demonstrating that several families of localized wave fronts are prevalent in both the photosphere and chromosphere, with only a subset aligning with VBI observations. We first describe two distinct families of waves whose sources are found in the the upper photosphere and low chromosphere. Synthetic spectra analysis shows that these waves are visible in the Ca II *K* channel but not in the *G*-band channel of DKIST. Next, we focus on the more extensively studied photospheric waves, whose sources typically lie beneath or near the photospheric surface. These photospheric waves would appear first in the *G*-band channel and, if they propagate high enough, potentially in the Ca II *K* channel. However, for such photospheric sources in MURaM, wave fronts are visible only in the *G*-band channel. In the upper photosphere, the wave amplitudes diminish and the wave fronts lose spatial coherence, rendering them undetectable in the Ca II *K* channel. Although the MURaM waves exhibit distinct characteristics compared to the observed waves and our sample size is small, our analysis suggests that the two newly identified families of waves, those that do not have their origin in the photosphere or below, are most analogous to those detected by the DKIST/VBI.

3.2. Wave Fronts and Wave Source Identification

Analysis of the velocity and pressure time series within the MURaM simulated atmosphere reveals the presence of multiple propagating circular and semicircular wave fronts (detailed statistics are discussed in a later section), many of which are observed in the synthesized Ca II *K* channel. The coaligned synthesized *G*-band channel shows no sign of these near the Ca II *K* wave front locations or the inferred excitation sites either before or after their occurrence in the Ca II *K* channel. Moreover, direct investigation of the simulation output (without spectral synthesis) finds no associated photospheric wave sources and only occasional very weak associated photospheric pressure perturbations 150 s either side of the Ca II *K* channel events. Further analysis, such as that described below for two example wave fronts, indicates that these ubiquitous wave fronts in the synthesized Ca II *K* time series have, as their source, dynamical events in the lower atmosphere (at the top of the convective overshoot region) or in the simulated chromosphere proper. The wave fronts do not propagate upward from the photosphere below nor do they propagate downward from the chromosphere into the underlying photosphere to a depth that would make them visible in the *G*-band channel. Finally, the analysis of individual excitation sites indicates that the observed wave fronts emerge from sites of localized pressure perturbations and exhibit a wave front speed close to the acoustic speed, although the role of magnetic field remains uncertain.

Figure 2 shows snapshots of two illustrative wave fronts in the MURaM simulated atmosphere that are observationally analogous to those in the DKIST/VBI image time series. Investigation of the underlying acoustic sources suggests that these two wave fronts originate with distinct physical processes. As illustrated by Figure 3, the stronger and more compact wave front (top row in Figure 2) initiates with a source at a height of about 900–1100 km above the photosphere. The wave front is visible in both the raw pressure-fluctuation field and its temporal difference (a three-difference filter as motivated and described in Bahauddin & Rast 2023). The difference filter significantly amplifies the signal and removes background contributions.

In this case, and for other sources found in the simulations at these heights, the chromospheric acoustic-source event appears to be an interaction between an upward propagating shock and downward moving chromospheric plasma (see the animation hosted by Figure 3 and the top two rows in the animation hosted by Figure 2). The initial pressure perturbation that develops into the shock can be traced back to the photosphere where it likely originates with *p*-mode coherence. Traveling upward through the temperature minimum and into the chromosphere, the acoustic pulse experiences pronounced steepening ultimately developing into a propagating shock, until in the chromosphere it encounters strongly downward moving plasma. The abrupt compression of the plasma in that collision gives rise to a new acoustic wave front that becomes visible in the Ca II *K* channel. Importantly, as upward shock propagation is pervasive in the low MURaM atmosphere, occurring every few minutes at any given location, such events are quite common, and secondary acoustic-wave radiation as a result of this type of dynamical interaction in the chromosphere appears to be an important shock dissipation mechanism at the height being observed.

The second acoustic wave front event illustrated in Figure 2 (bottom row) can be traced back to an origin near the temperature minimum, situated between the photosphere and the chromosphere at a height of approximately 400−600 km. Sources at this height originate with the interaction between upflows and downflows in the convective overshoot region. They are often located adjacent to strong granular upflows. When a downflow encounters an upflowing granule, collision between the two induces localized pressure fluctuations that radiate acoustic wave fronts, a Reynolds stress process reminiscent of the Lighthill mechanism (Lighthill 1952, 1954), although the Mach number of the flow is locally only approximately 1.2. Figure 4 and the bottom two rows in the animation hosted by Figure 2 illustrate this process, showing the pressure fluctuations in the upper row and their temporal difference in the bottom. As a strong downflow encounters a large, expanding granule, excess pressure builds up in the interface and acoustic waves are emitted in both the upward and downward directions (see the 1D velocity and velocity perturbation at $t = 1506$ s, plotted along the line of dynamic interaction, in the top two rows of the animation hosted by

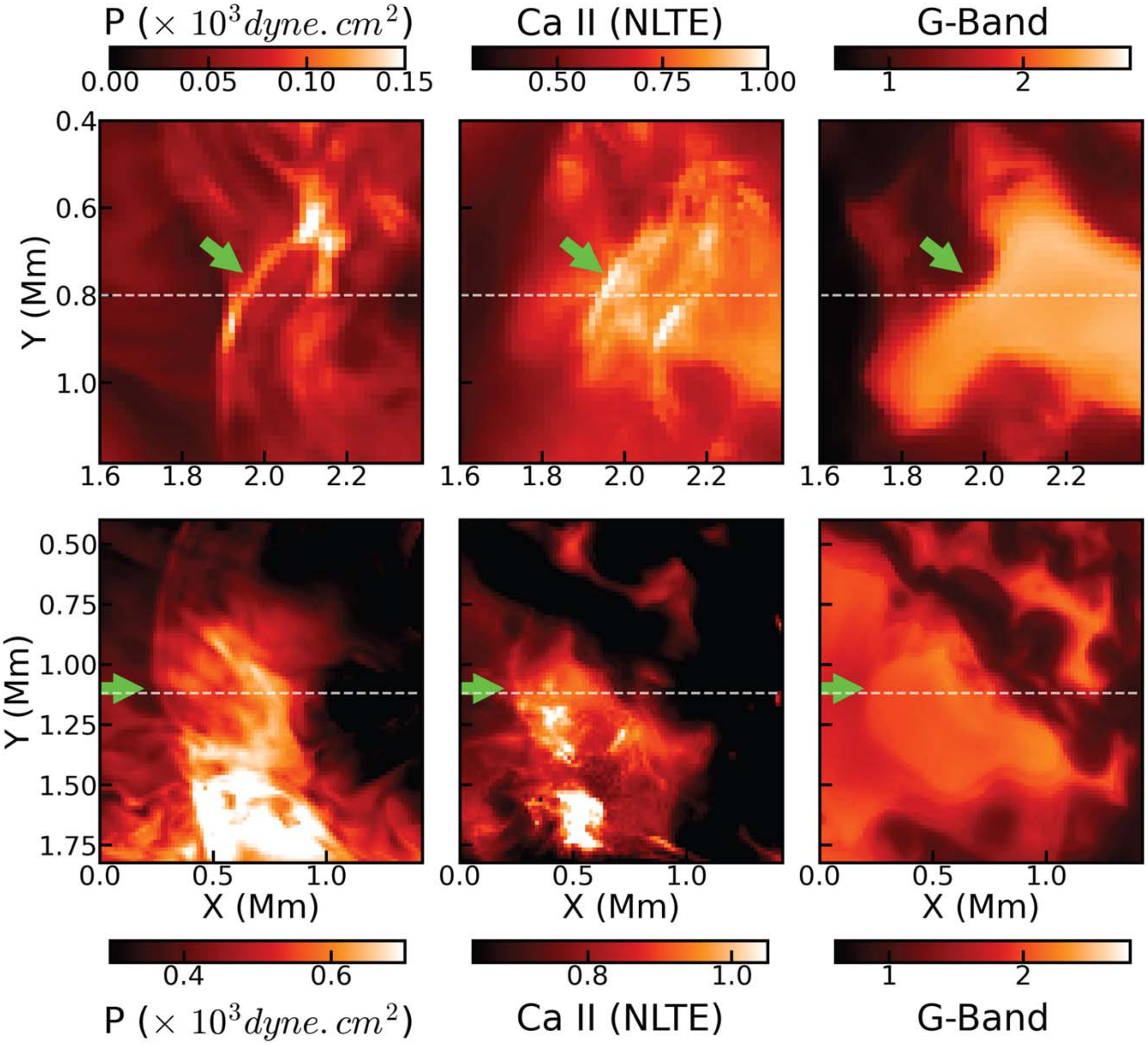

Figure 2. Two instances of a wave front are visible in the synthesized Ca II *K* (NLTE) channel but not in the *G*-band channel. Synthesized spectra for both channels are convolved with the DKIST/VBI filter profile to simulate observations. Green arrows in both rows indicate the location of the wave fronts. Due to the sources originating in the upper photosphere/chromosphere region, *G*-band images are delayed by 140 s for the chromospheric source (top) and 58 s for the upper photospheric source (bottom), accounting for the temporal delay of wave propagation in the stratified atmosphere. Dashed white lines indicate the vertical cut shown in the 11 s animation.

(An animation of this figure is available in the online article.)

Figure 4). These wave fronts are typically weaker than those produced by the shock/flow interactions previously discussed. They are most easily detected in the convective overshoot region (see the bottom two rows in the animation hosted by Figure 2 and the bottom row in the animation hosted by Figure 4), where the background atmosphere evolves more slowly than the wave and the difference filter is thus most effective. As the wave fronts propagate upward from the source, their spatial coherence is disrupted by the more vigorous background wavefield of the low chromosphere, and as they propagate downwards, their amplitudes diminish due to the steep stratification.

Pinpointing individual wave fronts requires low SNR that is challenging to achieve in observation, but within the 15 minute $\sim 5 \times 5$ arcsec^2 FOV DKIST observation window, we have successfully identified at least four distinct wave front events (see Appendix A). In the MURaM simulation, with better SNR, we can reliably track at least six wave fronts within a comparable temporal window and spatial FOV. While careful identification of the source properties requires spectral observations, and more robust statistical analysis requires longer time series with outstanding seeing, these numbers are not dissimilar, suggesting that chromospheric wave sources occur with a frequency of about 40 to 60 arcmin^{-2} minute^{-1}.

3.3. Photospheric Sources

Past theoretical analyses and observational studies of chromospheric waves have focused on acoustic sources in the upper convection zone of the Sun that are primarily associated with convective dynamics located in or below the solar photosphere. Many such sources can be identified in the MURaM simulations

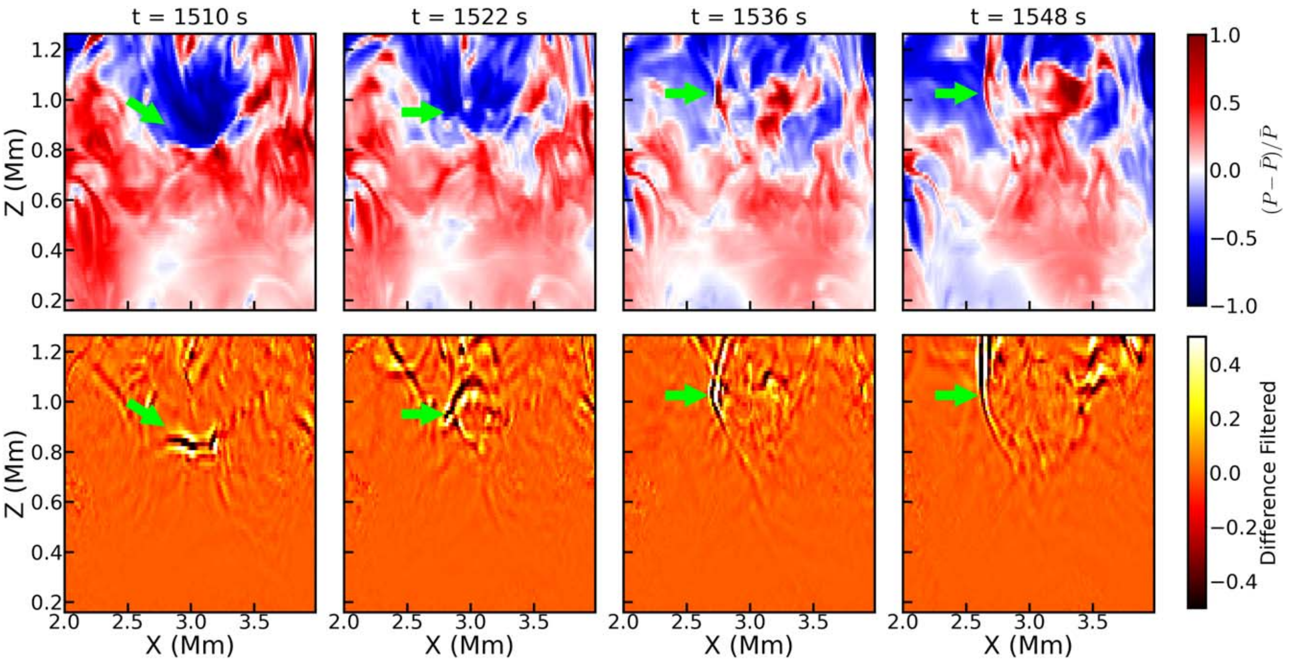

Figure 3. Local generation of a propagating wave front approximately 900 km above the photospheric surface. The top row presents the time series of pressure perturbations, depicting the generation of acoustic waves by the interaction between an upward propagating shock and a chromospheric downflow. In the bottom row, a three-difference-in-time filter is applied to enhance the visibility of the locally generated wave front (Bahauddin & Rast 2023). In both rows, the green arrows indicate the approximate locations of the wave front. Such events are quite common and appear to be an important shock dissipation mechanism in the chromosphere. The 4 s animation illustrates the dynamic $x-y$ planar evolution of wave front propagation at the height of 900 km.

(An animation of this figure is available in the online article.)

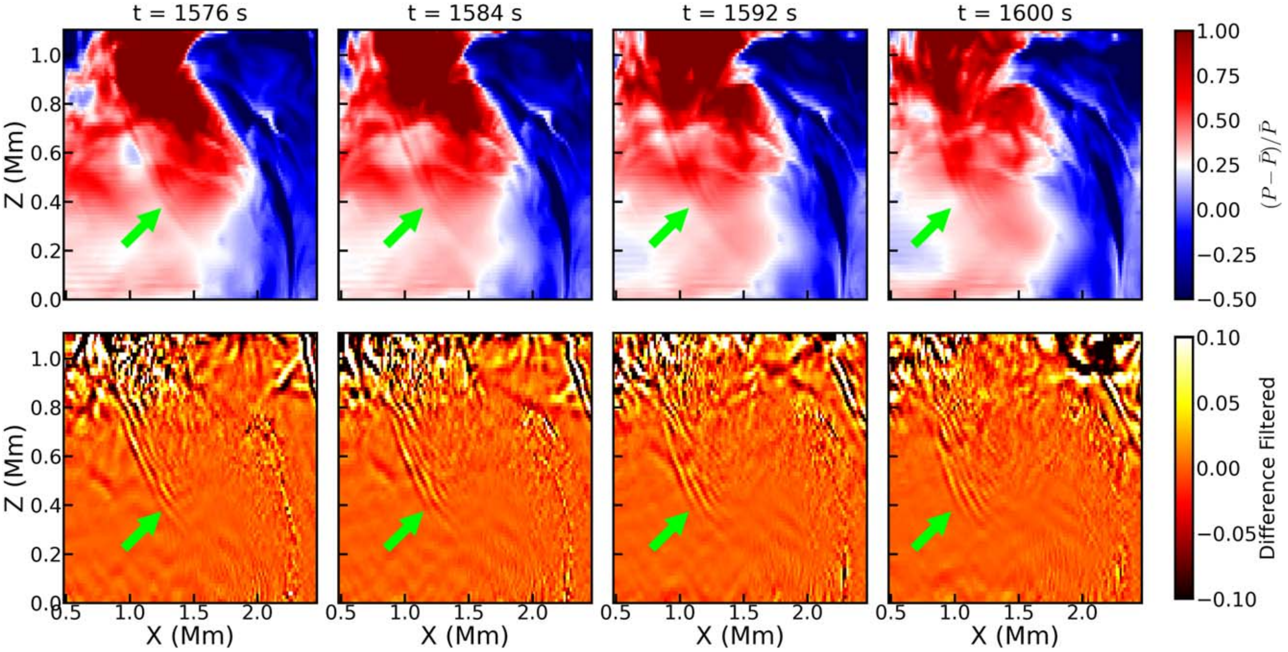

Figure 4. Generation of a acoustic wave front approximately 400 km above the photospheric surface. The top row presents the time series of pressure perturbations, depicting the generation of acoustic waves from the turbulent interaction between down-welling fluid and a large overshooting granule. In the bottom row, a three-difference-in-time filtering has been applied to enhance visibility, eliminating background contributions from the local wave perturbations (Bahauddin & Rast 2023). In both rows, green arrows highlight the locations of the wave fronts. The top two rows in the animation showcase the propagation of waves seen in the velocity field, highlighting the velocity perturbations along the line of dynamic interaction (13 s). The bottom row in the animation presents the dynamic evolution of wave front propagation in the $x-y$ plane at an altitude of 600 km (6 s).

(An animation of this figure is available in the online article.)

when temporal-difference filtering is employed (Bahauddin & Rast 2021, 2023). It is important to assess whether the waves generated by the photospheric sources propagate upward to chromospheric heights in the simulations and thus remain source candidates for at least some of the wave fronts observed in the DKIST/VBI Ca II *K* channel.

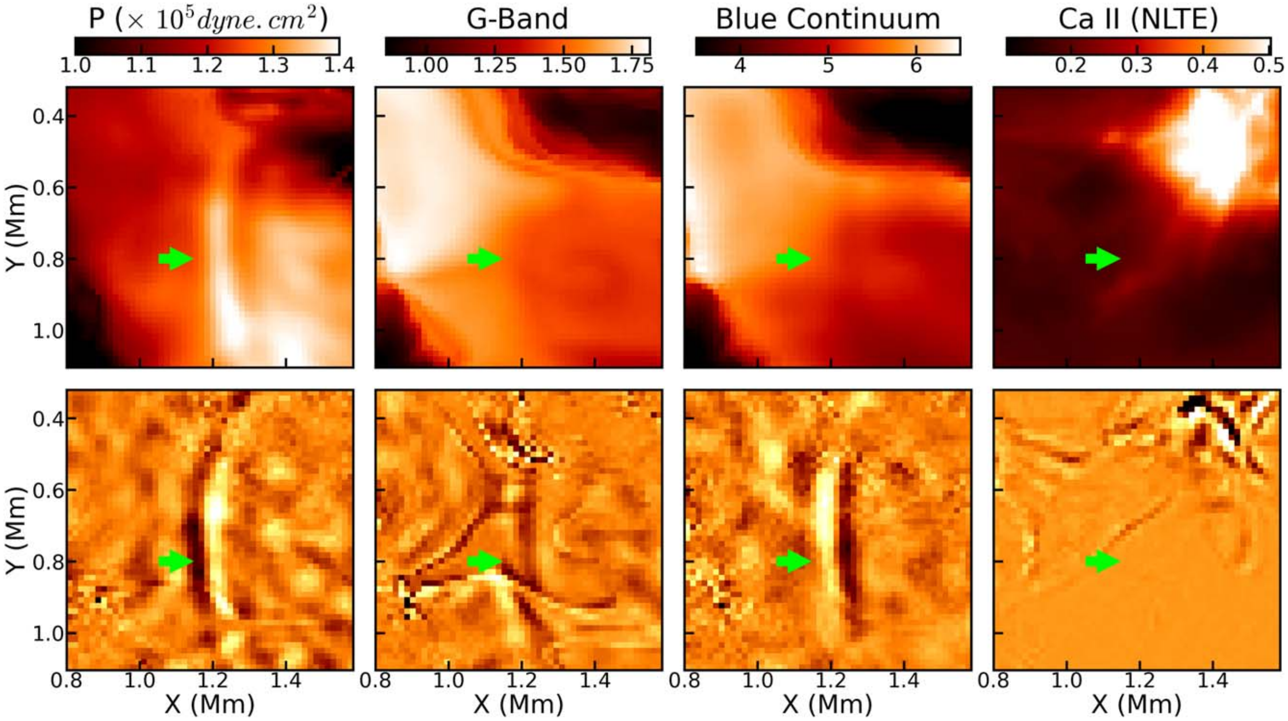

Figure 5. A local wave front originating from a subsurface source in the simulated solar photosphere. Top row: the wavefield is discernible in the pressure field, yet its visibility is limited in DKIST/VBI-resolution synthesized *G*-band, blue-continuum, and Ca II *K* (NLTE) channels due to weak SNR. Bottom row: to improve visibility, three-difference temporal filtering (Bahauddin & Rast 2021, 2023) is applied to denoise the images. Even in the temporal-difference images, the wavefield remains absent in the Ca II *K* channel. In both rows, green arrows highlight the location of the wave fronts.

Figure 5 presents a snapshot of a wave front produced by a subsurface acoustic source. Shown are the pressure perturbation in the solar photosphere and synthesized DKIST/VBI Ca II *K*, *G*-band, and blue-continuum signals along with a three-difference temporal filter of each. Since such photospheric sources originate in the solar surface, the Ca II *K* images shown in Figure 5 are delayed by 140 s, accounted for the wave traveling upward through a stratified atmosphere. Although the wave front is visible in the MURaM pressure field, it is barely discernible in the synthesized VBI channels without filtering, and even with filtering it is not seen in the Ca II *K* channel. Photospheric acoustic wave fronts, when of high enough amplitude, are observable in the synthesized *G*-band and blue-continuum channels but not in the Ca II *K* channel. This is precisely opposite of what the DKIST observations show, in which wave fronts are prominent in the VBI Ca II *K* channel but not seen in the *G* band, and suggests that individual impulsive excitation events in the upper convection zone and solar photosphere do not produce waves that reach the heights that the DKIST VBI Ca II *K* bandpass samples with sufficient amplitude to account for the Ca II *K* wave fronts observed. The difference between these individual source events and the upward propagating shocks, which do induce a secondary acoustic source in the chromosphere, lies in the fact that the latter are likely the result of *p*-mode coherence. Therefore, they are likely to have a significantly higher initial amplitude in the photosphere than the former.

4. Conclusion

This Letter presented an investigation of the observational signatures and underlying sources of the lower-chromospheric transient wave fronts found in data from the DKIST/VBI observations and in MURaM simulations. Spatially compact and temporally discrete wave fronts propagating away from source sites in the solar chromosphere are visible in the Ca II *K* DKIST/VBI channel but are absent from the coaligned *G*-band channel even when travel time delays are accounted for. This suggests that their origin is in the chromosphere proper.

We compare these observational findings with numerical simulations and confirm the persistent presence of propagating wave fronts in synthesized Ca II *K* time series. Further, analysis of the simulations suggests that these waves are acoustic in nature and originate from distinct physical sources and processes. Three such processes were identified: upward propagation of acoustic wave fronts from sources in and below the photosphere, turbulent excitation at the top of the convective overshoot region, and upward propagating shock interaction with downward moving plasma in the chromosphere leading to acoustic radiation and shock dissipation. Only the latter two show the characteristic Ca II *K* presence and *G*-band absence of the observed transients.

The transient events we have identified have significant diagnostic potential. They promise a new helioseismic avenue for the high-resolution inference of the solar atmospheric properties at different heights (Bahauddin & Rast 2023). The discovery of acoustic radiation from upward propagating shocks may be a particularly significant result of this work. It may provide a way to directly investigate *p*-mode energy deposition in the lower solar atmosphere. In this regard, it is important to understand some critical differences between the observed and simulated wave fronts. Although the observed wave fronts exhibit similar SNR (∼3) against the background as those found in the simulations, they traverse a greater distance before becoming indistinguishable from it. Consequently, the observed wave fronts become longer in extent as the wave front expands. They also show greater cross-sectional widths than those in the simulations, which is likely related to the details of their excitation. Together these differences suggest that wave front sources in the Sun have larger amplitudes and durations, and/or that wave damping in the solar atmosphere is weaker than it is in the simulations.

The observed wave fronts also propagate with a higher speed (approximately $14\,\mathrm{km\,s^{-1}}$) than do those in the simulation ($\sim 9\,\mathrm{km\,s^{-1}}$). This may reflect difference in the magnetized nature of the real and simulated chromosphere or may be due to differences in the advection of the wave fronts by the local flows. The mean horizontal velocity amplitude in the MURaM atmosphere at the formation height of Ca II *K* has a value of $2\,\mathrm{km\,s^{-1}}$, while the average speed of sound at those heights is approximately $7\,\mathrm{km\,s^{-1}}$. The sum of these is consistent with the observed wave front velocity in the simulation which is about $9\,\mathrm{km\,s^{-1}}$. If the observed wave front speeds are thus influenced by their advection, there is an implied correlation between the direction of wave front propagation and background motions. This correlation may be due to an observational bias, as the wave fronts could be more visible in areas with smoother horizontally diverging flows. Such an effect is evident in the previous analysis of photospheric wave fronts (Bahauddin & Rast 2023). Interestingly, the wave propagation speeds of the slow and fast modes of magnetoacoustic waves in the MURaM low chromosphere are 6.5 and $9.2\,\mathrm{km\,s^{-1}}$, respectively, the latter also close to the observed wave front velocity in the simulation. However, the role of magnetism remains uncertain in our observations since polarization measurements at this cadence are currently unavailable. Unraveling these contributions is a key goal for future research.

While conducting our study, a possible alternative interpretation of the wave fronts became apparent, fine-scale chromospheric fibrils (da Silva Santos et al. 2023). Fibrils are frequently observed in the Ca II *K* core and their motions may account for propagating narrow structures in the time series. However, the temporal dynamics of fibrils are notably slower than the features we examined, and they are not expected to exhibit expanding wave front–like propagation from a source site at a speed close to the sound speed. It is crucial to acknowledge, however, that amidst the background chromospheric wavefield, discerning whether a propagating front results from a localized acoustic source or arises from the spatially distributed evolving pressure field is challenging. This task is even more difficult than identifying photospheric wave fronts, because in the chromosphere there is little timescale separation between the background "noise" and the signal on which to base the filtering (Bahauddin & Rast 2023).

DKIST observation of wave front propagation in the solar atmosphere promises significant advancement in our understanding of both the complex source dynamics and the background through which the source generated wave fronts travel. With careful study, the presence of acoustic source sites in the deep solar photosphere, in the convective overshoot region, and in the lower solar chromosphere will allow ultralocal helioseismic inference of the atmospheric properties, reassessment of wave-heating and momentum transport mechanisms as a function of height, and increased confidence in our ability to model this critical region of the solar atmosphere.

Acknowledgments

The authors thank Han Uitenbroek for valuable guidance and advice on the synthesis of the *G*-band spectrum. This work was partially supported by the National Science Foundation Award No. 2206589 and the National Solar Observatory's DKIST Ambassadors program. The National Solar Observatory is a facility of the National Science Foundation operated under Cooperative Support Agreement No. AST-1400450. This research was also supported by the International Space Science Institute (ISSI) in Bern, through ISSI International Team project 502 (WaLSA: Waves in the Lower Solar Atmosphere). The simulation material is based upon work supported by the NSF National Center for Atmospheric Research, which is a major facility sponsored by the U.S. National Science Foundation under Cooperative Agreement No. 1852977.

Facility: DKIST

Appendix A
Occurrence of Wave Fronts in DKIST/VBI

Four observed wave fronts originating from sources discussed in this study are illustrated in Figure A1 in order to compare their rate of occurrence with simulation. These wave fronts exhibit consistent characteristics regarding their extension, cross-sectional shape, and propagation velocities.

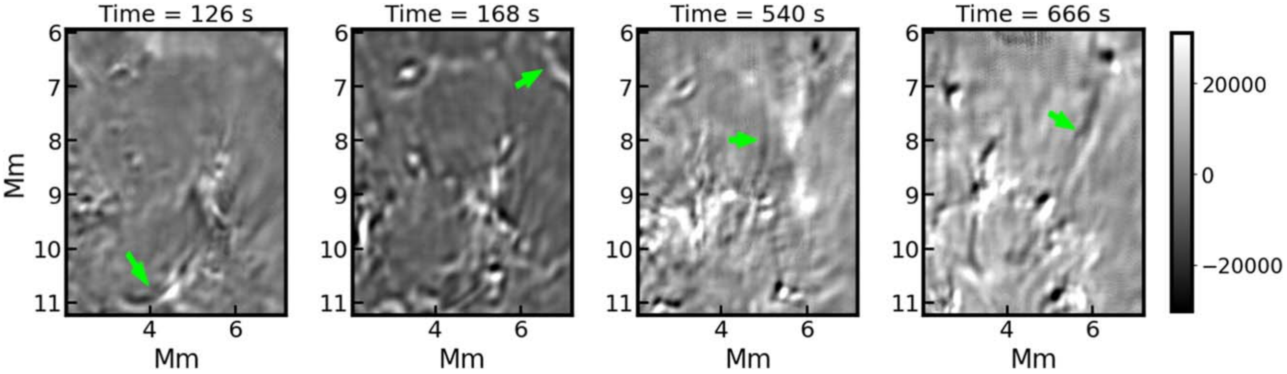

Figure A1. Four local wave fronts identified during a 15 minute observation window by DKIST/VBI in a $\sim 5 \times 5$ arcsec^2 field of view. Green arrows mark the spatial location of these wave fronts.

Appendix B
Radiative Transfer

The MURaM atmosphere is transformed to generate a SNAPI-compatible cube for simulating the Ca II K channel and an RH-compatible cube for simulating the G band. In order to forward model Ca II K channel, SNAPI resolves spectra across 601 wavelength points spanning from 393.03 to 393.63 nm. The synthesis of the G-band channel, with its broader filter FWHM, which incorporates numerous molecular and atomic lines, requires RH to forward model spectra across 3001 wavelength points ranging from 429.0 to 432.0 nm. In addition, the molecular files of RH is populated appropriately to account for the absorption and scattering by the abundant molecules (such as CH) present in the solar photosphere.

The simulation of the VBI response for each channel involves the application of a filter profile across the spectrum. The filter profiles for the Ca II K and G-band channels are modeled using the equation: profile $= \frac{1}{1+t}$, where $t = \left(|\lambda - \lambda_0| / \frac{\Delta}{2}\right)^{2L}$. Here, λ_0 is the center wavelength, Δ is the FWHM of the channels, and $L =$ cavity length ($L = 2$ is used for both Ca II K and for the G band).

ORCID iDs

Shah Mohammad Bahauddin https://orcid.org/0000-0003-0016-5377
Mark P. Rast https://orcid.org/0000-0002-9232-9078
Ivan Milic https://orcid.org/0000-0002-0189-5550
Matthias Rempel https://orcid.org/0000-0001-5850-3119
Peter H. Keys https://orcid.org/0000-0001-8556-470X

References

Abbasvand, V., Sobotka, M., Švanda, M., et al. 2020, A&A, 642, A52
Bahauddin, S. M., & Rast, M. P. 2021, ApJ, 915, 36
Bahauddin, S. M., & Rast, M. P. 2023, ApJ, 955, 31
Bello González, N., Franz, M., Martínez Pillet, V., et al. 2010, ApJL, 723, L134
Biermann, L. 1946, NW, 33, 118
Chaplin, W. J., Elsworth, Y., Isaak, G. R., et al. 1998, MNRAS, 298, L7
da Silva Santos, J. M., Reardon, K., Cauzzi, G., et al. 2023, ApJL, 954, L35
Ermolli, I., Criscuoli, S., Uitenbroek, H., et al. 2010, A&A, 523, A55
Fischer, C., Woeger, F., Rimmele, T., et al. 2023, AAS/Solar Physics Division Meeting, 55, 407.03
Fleck, B., Couvidat, S., & Straus, T. 2011, SoPh, 271, 27
Fontenla, J. M., Avrett, E. H., & Loeser, R. 1993, ApJ, 406, 319
Gabriel, M. 1995, A&A, 299, 245
Goldreich, P., Murray, N., & Kumar, P. 1994, ApJ, 424, 466
Goode, P. R., Strous, L. H., Rimmele, T. R., & Stebbins, R. T. 1998, ApJL, 495, L27
Hansteen, V. H., Carlsson, M., Cargill, P., & Vlahos, L. 2009, in Turbulence in Space Plasmas, ed. Plasmas, 778 (Berlin: Springer), 129
Hansteen, V. H., De Pontieu, B., Rouppe van der Voort, L., van Noort, M., & Carlsson, M. 2006, ApJL, 647, L73
Kalkofen, W. 2007, ApJ, 671, 2154
Kitiashvili, I. N., Kosovichev, A. G., Mansour, N. N., Wray, A. A., & Sandstrom, T. A. 2019, ApJ, 872, 34
Lighthill, M. J. 1952, RSPSA, 211, 564
Lighthill, M. J. 1954, RSPSA, 222, 1
Lindsey, C., Buitrago-Casas, J. C., Martínez Oliveros, J. C., et al. 2020, ApJL, 901, L9
Lindsey, C., & Donea, A.-C. 2013, JPhCS, 440, 012044
Milić, I., & van Noort, M. 2018, A&A, 617, A24
Molnar, M. E., Reardon, K. P., Cranmer, S. R., Kowalski, A. F., & Milić, I. 2023, ApJ, 945, 154
Musielak, Z. E., Rosner, R., Stein, R. F., & Ulmschneider, P. 1994, ApJ, 423, 474
Nigam, R., Kosovichev, A. G., Scherrer, P. H., & Schou, J. 1998, ApJL, 495, L115
Nordlund, A. 1982, A&A, 107, 1
Perdomo García, A., Vitas, N., Khomenko, E., et al. 2023, A&A, 675, A160
Philidet, J., Belkacem, K., & Goupil, M. J. 2021, A&A, 656, A95
Philidet, J., Belkacem, K., & Goupil, M. J. 2022, A&A, 664, A164
Rast, M. P. 1995, ApJ, 443, 863
Rast, M. P. 1999, ApJ, 524, 462
Rast, M. P., & Bogdan, T. J. 1998, ApJ, 496, 527
Rempel, M. 2014, ApJ, 789, 132
Rempel, M., Schüssler, M., & Knölker, M. 2009, ApJ, 691, 640
Rimmele, T. R., Goode, P. R., Harold, E., & Stebbins, R. T. 1995, ApJL, 444, L119
Rimmele, T. R., Warner, M., Keil, S. L., et al. 2020, SoPh, 295, 172
Roth, M., Franz, M., Bello González, N., et al. 2010, ApJL, 723, L175
Rybicki, G. B., & Hummer, D. G. 1991, A&A, 245, 171
Samadi, R., Georgobiani, D., Trampedach, R., et al. 2007, A&A, 463, 297
Samadi, R., & Goupil, M. J. 2001, A&A, 370, 136
Schwarzschild, M. 1948, ApJ, 107, 1
Severino, G., Magrì, M., Oliviero, M., Straus, T., & Jefferies, S. M. 2001, ApJ, 561, 444
Skartlien, R., & Rast, M. P. 2000, ApJ, 535, 464
Stein, R. F. 1967, SoPh, 2, 385
Stein, R. F. 1991, in Challenges to Theories of the Structure of Moderate-Mass Stars, ed. D. Gough & J. Toomre, 388 (Berlin: Springer), 195
Straus, T., Severino, G., Deubner, F. L., et al. 1999, ApJ, 516, 939
Strous, L. H., Goode, P. R., & Rimmele, T. R. 2000, ApJ, 535, 1000
Uitenbroek, H. 2001, ApJ, 557, 389
Vögler, A., Shelyag, S., Schüssler, M., et al. 2005, A&A, 429, 335
Wöger, F., Rimmele, T., Ferayorni, A., et al. 2021, SoPh, 296, 145
Wöger, F., von der Lühe, O., & Reardon, K. 2008, A&A, 488, 375
Yadav, N., Cameron, R. H., & Solanki, S. K. 2021, A&A, 652, A43
Zhou, Y., Asplund, M., & Collet, R. 2019, ApJ, 880, 13
Zhou, Y., Asplund, M., Collet, R., & Joyce, M. 2020, MNRAS, 495, 4904